Frictional strength and stability of greywacke fault zones

Lead Investigator:

Dr Carolyn Boulton, Te Herenga Waka Victoria University of Wellington

Research Team:

Associate Professor André Niemeijer, Utrecht University, the Netherlands

Frontispiece: Greywacke exposed in the hanging wall of the Elliott Fault, Acheron River. Photograph by C Boulton.

Acknowledgements
We acknowledge research funding from Toka Tū Ake EQC which supported the field research and laboratory analyses. We also thank Professor Andy Nicol at the University of Canterbury for help with mapping and sample collection on the Leader Fault. Susan Ellis and Stephen Bannister (GNS Science) and Teak Jin Chua (MSc student at Victoria University of Wellington) provided insightful discussions and are participating in an ongoing collaboration that applies the experimental results to understanding the seismic behaviour of greywacke faults in the Wellington region.

Executive Summary

Aotearoa New Zealand sits astride the Australian-Pacific plate boundary. As the Australian and Pacific plates are forced to slide past each other, strain energy accumulates in the rocks on either side of locked faults. If the locked faults slide suddenly in earthquakes, the stored strain energy results in movement on the faults and radiated seismic waves, which can cause damaging ground motions. In Aotearoa, faults are most commonly located in basement sandstone and siltstone rocks of the Torlesse Composite Terrane. These rocks are colloquially termed “greywacke”. The frictional strength of basement sandstone and siltstone, as well as the propensity of these rocks to host earthquakes, are important input parameters in the seismic hazard models that are used to forecast earthquakes and their effects. By performing friction experiments on sandstone and siltstone samples collected from a fault that ruptured in the 2016 Kaikōura earthquake, we found that at shallow depths (typically < 10 km depth), the siltstone is frictionally weaker than the sandstone. However, at depths > 10 km, both rock types have approximately the same frictional strength and this strength is consistent with a majority of rock types studied worldwide.

At depths > 10 km, both rock types are also frictionally unstable, meaning that they are likely to nucleate earthquakes if there is enough driving stress to overcome the frictional resistance to sliding. As temperature increases, our experiments show that both rocks become frictionally stable again, and the temperature range that corresponds to the change from frictionally unstable to frictionally stable is called the seismic-to-aseismic transition. Earthquakes are unlikely to nucleate below the seismic-to-aseismic transition, so this depth fundamentally limits the area of a fault that can rupture in an earthquake and thus the maximum moment magnitude able to be generated. In Torlesse Composite Terrane sandstone and siltstone, the seismic-to-aseismic transition temperature depends on rock type and sliding velocity. For the slowest sliding velocities tested, the transition happens at temperatures above 350°C in the siltstone and 400°C in the sandstone. Correlating these temperatures with absolute depths requires additional constraints on how temperature changes with depth, which varies in different regions across Aotearoa New Zealand.

Technical Abstract

Hydrothermal friction experiments were performed on Torlesse Composite Terrane sandstone and siltstone sampled from the footwall and immediate hanging wall of the North Leader Fault, a fault that ruptured in the 2016 Mw 7.8 Kaikōura earthquake. Experiments were performed in a rotary shear apparatus at effective pressures of 75 MPa, temperatures of 20–600°C, and velocities of 0.01–100 µm s^{-1} in order to determine the friction coefficient and velocity dependence of friction. Results show that both sandstone and siltstone exhibit velocity-weakening behaviour and have Byerlee values (μ = 0.6–0.8) of sliding friction at temperatures of ca. 250–400°C. At lower temperatures, the siltstone is frictionally weaker (μ = 0.33–0.53) than the sandstone (μ = 0.55–0.64) and exhibits velocity-strengthening behaviour, which inhibits earthquake rupture nucleation.

The low temperature velocity-strengthening to velocity-weakening transition, interpreted to represent the uppermost depth of the seismogenic zone, defined as the zone in which earthquakes are able to nucleate, depends on lithology and sliding velocity. At the lowest velocities imposed (0.01–0.03 µm s^{-1}), the transition from velocity-strengthening to velocity-weakening occurs at 150°C in the sandstone and 200°C in the siltstone. At the highest sliding velocities investigated (30–100 µm s^{-1}), the transition temperature increases to 200°C in the sandstone and 300°C in the siltstone.

The high temperature velocity-weakening to velocity-strengthening transition, interpreted to represent the deepest portion of the seismogenic zone, also depends on lithology and sliding velocity. At the lowest velocities imposed (0.01–0.03 µm s^{-1}), the transition from velocity weakening to velocity strengthening occurs at 400°C in the sandstone and 350°C in the siltstone. At the highest sliding velocities investigated (30–100 µm s^{-1}), the temperature of the transition increases to over 500°C in the sandstone and 450°C in the siltstone. Experimental results show that frictional stability depends on sliding velocity; extremely slow sliding velocities (0.01-0.03 µm s^{-1}) correspond with the narrowest temperature range (200–300°C) of velocity-weakening behaviour and unstable slip in *both* the sandstone and siltstone.

The hypocentres of the Mw 7.1 Darfield and the 2016 Mw 7.8 Kaikōura were located at ~10 km and ~12.5 km depth, respectively. Using the average Canterbury geothermal gradient (20°C km^{-1}), these hypocentral depths correspond to the temperature interval over which both the sandstone and siltstone exhibited the velocity-weakening behaviour requisite for earthquake nucleation at all imposed sliding velocities.

Keywords

Earthquakes, quantifying hazards, fault mechanics, frictional properties, Torlesse Composite Terrane bedrock

Introduction

The frictional strength and stability of rocks within faults fundamentally affects how and where earthquakes nucleate, propagate, arrest and radiate energy (e.g., Scholz, 2002). Across Aotearoa New Zealand, multiple large-magnitude earthquakes have ruptured greywacke fault zones (Nicol et al. 2016). Notably, the recent 2010 M_w 7.1 Darfield and 2016 M_w 7.8 Kaikōura Earthquakes were both hosted by faults crosscutting (and subparallel to) the sandstone and siltstone rocks that comprise the Torlesse Composite Terrane, the basement rocks colloquially referred to as greywacke (e.g., Mortimer 2004; Quigley et al. 2012; Litchfield et al., 2018; Nicol et al., 2018). In this study, we measured – for the first time – the frictional strength and stability of Torlesse Composite Terrane sandstone and siltstone, and we quantified the mineralogy of the samples studied.

Research on the frictional properties of New Zealand's basement rocks provides data directly relevant to ongoing, interdisciplinary efforts to mitigate seismic risk. In particular, frictional strength and stability are key input parameters in new physics-based models of earthquakes (e.g., Shaw et al., 2022), which are increasingly being used to assess hazard by forecasting fault rupture, ground motion shaking, liquefaction, and tsunami. Frictional strength and stability are also used to identify and physically understand the maximum depth of seismic rupture, a key parameter within the New Zealand Seismic Hazard Model (NZ NSHM) (e.g., Ellis et al., 2021). Along with fault length, the maximum depth of seismic rupture governs the total fault area that can rupture in an earthquake, which is used in the calculation of earthquake moment magnitude (Hanks and Kanamori 1979).

The M_w 7.8 Kaikōura Earthquake nucleated on The Humps Fault in North Canterbury (ca. 30 km southwest of the study area) at a depth of 12.5 ± 5.8 km (Nicol et al. 2018; Chamberlain et al. 2021). The earthquake propagated to the northeast, rupturing over 20 faults before finally arresting on the Needles Fault beneath Cook Strait (Litchfield et al. 2018). At the ground surface, these faults ruptured Late Jurassic to Early Cretaceous sandstone and siltstone of the basement Torlesse Composite Terrane together with overlying Cretaceous and younger sedimentary strata. For the hydrothermal frictional properties experiments and mineralogical analyses documented in this study, basement rock samples were collected from the sinistral-reverse Leader Fault. During the Kaikōura Earthquake, the Leader Fault accommodated up to 2.5 ± 0.15 m of horizontal offset and 3.5 ± 0.5 m of vertical offset, with a mean horizontal to vertical slip ratio of 1.4 ± 1.0 (Nicol et al. 2018) (Figure A1.1).

In the region of study, bedding in the Torlesse Composite Terrane sandstone and siltstone generally strikes north-south sub-parallel to the strike of the Leader Fault (Nicol et al., 2018), suggesting that, at the surface, the fault may have partly utilised bedding heterogeneity (Figure A1.2). For the mineralogical analysis and friction experiments, samples of greywacke sandstone (LF8, LF10) and siltstone (LF6, LF9) were collected from the immediate hanging wall and footwall of the North Leader Fault at Campbell (Figure A1.2). Torlesse Composite Terrane sandstone is widely referred to as greywacke (e.g., Mackinnon 1983) in older literature, but here we use sandstone to describe these rocks. Similarly, older literature refers to finer-grained rocks in the Torlesse Composite Terrane as argillite, but here we use the term siltstone. New quantitative X-ray diffraction analyses show that the finer-grained siltstone samples contain a larger proportion of frictionally weak phyllosilicate minerals than the coarser-grained sandstone samples (Table A2.1).

As documented in Appendices 2 and 3, mineralogical variations in the sandstone and siltstone correspond to differences in the frictional strength and stability (i.e., the frictional properties). To measure the frictional properties of these two rock types, hydrothermal friction experiments were performed in a rotary shear apparatus at effective pressures of 75 MPa, temperatures of 20–600°C, and velocities of 0.01–100 μm s^{-1} (Appendix 3). Results show that both sandstone and siltstone have Byerlee values (μ = 0.6–0.8) of sliding friction at temperatures of ca. 250–400°C (cf. Byerlee 1978). At lower temperatures, the siltstone is frictionally weaker (μ = 0.33–0.53) than the sandstone (μ = 0.55–0.64). Because the siltstone is frictionally weaker than the sandstone at lower temperatures, which correspond to shallower depths, slip on faults containing siltstone or siltstone-derived fault rocks will be mechanically favourable. In addition, the relative weakness of the siltstone means that faults in siltstone can slip at a wider range of angles to the maximum principal stress than faults formed in sandstone (Sibson 1985). This analysis assumes that faults slip when the Mohr-Coulomb failure criterion is met, and it assumes that pore fluid pressure is equal in faults formed within sandstone and siltstone (Hubbert and Rubbey 1959; Sibson 1985). At a constant applied normal stress, variations in fault strength can occur because of variations in fault rock frictional properties, which are strongly correlated with mineralogy (e.g., Byerlee 1978; Moore and Lockner, 2004). Variations in pore fluid pressure (Hubbert and Rubey 1959) and cohesion (Byerlee 1978; Sibson 1974) can also influence fault strength, but these properties were not explored in our research.

Over time, acceleration can trigger an earthquake (a frictional instability) within fault rocks prone to unstable, seismic slip (Scholz 2002). The rate-and-state friction (RSF) equations describe how a simulated fault or fault gouge responds to a quasi-instantaneous change in velocity (Figure 1). In the context of a spring-block slider model, in which the stability of sliding is controlled by RSF friction, a positive value of (*a*–*b*) results in stable sliding. Regions of faults composed of rocks with positive values of (*a*–*b*) are stable, that is, the faults tend to creep. Frictional instabilities require a negative value of (*a*–*b*). Numerous experimental studies of natural and analogue fault rocks have reported rate-and-state friction parameter (*a*–*b*) values and how (*a*–*b*) varies with temperature, pressure, and mineralogy (e.g., Dieterich 1979; Ruina 1982; Niemeijer et al. 2016; Boulton et al. 2019).

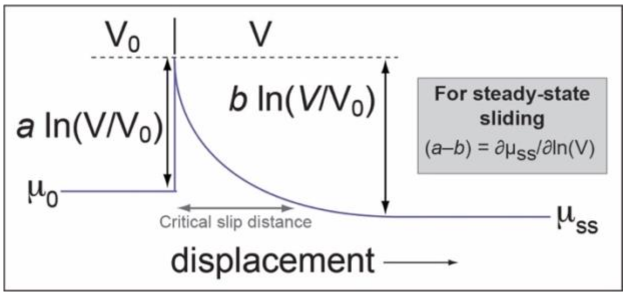

***Figure 1**. Schematic illustration of a velocity step from a lower (V_0) to a higher (V) sliding velocity. Over a critical slip distance, the coefficient of friction (μ_0) evolves to a new steady-state value (μ_{ss}). At steady-state, the RSF parameter (a–b) is equal to the difference in the steady-state friction coefficient divided by the natural logarithm of the sliding velocity over the reference sliding velocity. For details, see Appendix 3.*

Results from hydrothermal friction experiments performed to measure the RSF friction parameters (*a*–*b*) of the North Leader Fault siltstone and sandstone samples are documented in Appendix 3. The low temperature transition from positive (*a*–*b*), termed velocity strengthening, to negative (*a*–*b*), termed velocity weakening, was obtained for both lithologies. This temperature is interpreted to represent the lowest temperature, and shallowest depth, that earthquakes are able to nucleate. At the lowest velocities imposed (0.01–0.03 μm s^{-1}), the transition from velocity-strengthening to velocity-weakening occurs at 150°C in the sandstone and 200°C in the siltstone. At the highest sliding velocities investigated (30–100 μm s^{-1}), the transition temperature increases to 200°C in the sandstone and 300°C in the siltstone.

The high temperature transition from velocity weakening to velocity strengthening, interpreted to represent the deepest portion of the seismogenic zone, also depends on lithology and sliding velocity. At the lowest velocities imposed (0.01–0.03 μm s^{-1}), the transition from velocity weakening to velocity strengthening occurs at 400°C in the sandstone and 350°C in the siltstone. At the highest sliding velocities investigated (30–100 μm s^{-1}), the temperature of the transition increases to over 500°C in the sandstone and 450°C in the siltstone. Experimental results show that frictional stability depends on sliding velocity; extremely slow sliding velocities (0.01-0.03 μm s^{-1}) correspond with the narrowest temperature range (200–300°C) of velocity-weakening behaviour and unstable slip in *both* the sandstone and siltstone.

In the hydrothermal friction experiments, we assumed a constant normal stress and explore how transitions between velocity strengthening and velocity weakening varied as a function of rock type, sliding velocity, and temperature. Correlating the temperatures at which the (shallow) transition from velocity strengthening to velocity weakening and the (deep) transition from velocity weakening to velocity strengthening occur with absolute depths would require additional constraints on regional geothermal gradients, which vary across Aotearoa New Zealand (e.g., Allis et al. 1998; Ellis et al. 2021).

Discussion

The sliding friction of the Leader Fault samples depends critically on the amount of phyllosilicates present and thus on whether the sample is derived from sandstone or siltstone. The contrast in friction is greatest at room temperature and low velocity: it varies from μ=0.33 (LF6) to μ=0.55 (LF8 and LF10). The low value for LF6 is higher than the sliding friction of pure montmorillonite under comparable conditions (μ = ~0.15-0.20; Morrow et al. 2017) and is comparable to pure illite/muscovite (μ = 0.38-0.46; Morrow et al. 1992; Moore and Locker 2004; Behnsen and Faulkner 2012). The sliding friction of LF8 and LF10 is slightly lower than that of pure quartz (μ=0.6-0.65, cf. Marone et al. 1990).

As temperature increase, the contrast in sliding friction between the two lithologies diminishes. At a temperature of 450°C, the order is reversed: the siltstone samples have high friction than the sandstone samples, but the difference is relatively small ($\Delta\mu$ < 0.15). The temperature at which the siltstone samples show higher friction than the sandstone samples depends on velocity and sliding history. In the experiments performed at the lowest velocities, the siltstone is frictionally stronger than the sandstone at a temperature of 350°C. Increases in sliding friction with temperature have been observed in previous hydrothermal experiments on illite-rich samples (Moore et al. 1986; den Hartog et al. 2012).

The velocity dependence of friction, quantified using the RSF parameter (*a*–*b*), of all investigated samples varies with velocity and temperature. The RSF parameter (*a*–*b*) transitions from mostly positive values at room temperature to almost exclusively negative values at T = 300°C and back to mostly positive values at T = 500°C. The exact temperature at which both transitions occurs depends on the imposed sliding velocity. These three regimes of distinct velocity dependence of friction, positive (*a*–*b*)-negative (*a*–*b*)-positive (*a*–*b*), have been recognized in previous experimental studies of rock friction (e.g. Chester and Higgs 1992; Blanpied et al. 1995; den Hartog et al. 2013; Verberne et al. 2015), as well as for samples of the Alpine Fault, the largest fault on the South Island (Niemeijer et al. 2016).

A possible explanation for this behaviour can be found in the models proposed by Niemeijer and Spiers (2007), den Hartog and Spiers (2014), and Chen and Spiers (2016). In these models, a competition between slip-dependent granular flow and time-dependent, thermally activated mechanisms can explain changes in frictional stability. At low temperature or high velocity, dilatant granular flow dominates, and porosity is at a maximum value, analogous to the critical state in soil mechanics. In this regime, the velocity dependence of friction is solely controlled by the velocity dependence of friction between grains, which is typically velocity strengthening (Chen and Spiers 2016). At high temperature and low velocity, thermally activated mechanisms are can occur, primarily diffusive mass transfer processes such as pressure solution creep (cf. Rutter 1976; Rutter and Mainprice 1979), and these processes cause the gouge to lose porosity and densify. At high temperature and low velocity, displacement can be accommodated entirely via viscous flow processes such as pressure solution creep, which is strongly velocity strengthening. In the intermediate, velocity-weakening regime, both dilatant granular flow and pressure solution creep processes operate at comparable rates so that the steady-state porosity is controlled by the competition between granular flow and viscous flow. Velocity-dependent changes in porosity can then be linked microphysically to changes in the coefficient of sliding friction and thus the RSF parameter (*a*–*b*) (cf. Figure 1) (Niemeijer and Spiers 2007).

Hydrothermal friction data obtained from the Leader Fault are consistent with this interpretation. As temperature increases, velocity-weakening behaviour first appears at the lowest velocity. As temperature increases further, velocity strengthening again appears first at the lowest velocity (Figure A3.3). It is likely that some form of fluid-assisted pressure solution creep is the time- and temperature-dependent mechanism that is responsible for the observed transitions in the RSF parameters (e.g., Chen & Spiers 2016). It is interesting to note that the transition temperature of velocity-weakening to velocity-strengthening behaviour, which corresponds to the bottom of the seismogenic zone, is lower for the siltstone samples than for the sandstone samples. This could be a consequence of the larger phyllosilicate content in those samples. Phyllosilicates can facilitate the transition from frictional granular flow processes to viscous flow processes by either forming a weak foliation (Niemeijer 2018) or by enhancing the kinetics of diffusion of solutes (Renard et al. 2001). Another possible explanation is that the transition is controlled by the relative content of quartz and feldspars, which have different dissolution rates and solubilities. Further research is needed to explain how the strength, solubility, grain size, and distribution of primary, secondary and tertiary phases (i.e., minerals) affect deformation processes in polymineralic gouges.

We have not yet been able to identify the deformation mechanisms that control the observed temperature-dependent transitions in frictional stability or to verify whether natural fault gouges show evidence for the operation of these mechanisms. The transition temperatures of frictional stability, based on the experimental data obtained at the lowest sliding velocities, are 200 and 350°C for the siltstone samples, and for sandstone samples these temperatures are 150 and 400°C. It is important to note here that at ≤200°C, the siltstone samples are weaker than the sandstone samples, and the opposite is true at >350°C. Experimental data gathered at the slowest sliding velocities (0.01-0.03 μm s^{-1}) suggest that earthquake rupture nucleation can occur within both sandstone and siltstone over a depth interval corresponding to the temperature range 200–300°C. The range quoted corresponds to when the RSF parameter (a–b) is negative. In the siltstone, the low temperature transition back to positive (a–b) occurs between 150°C and 200°C in the siltstone, and the high temperature transition back to positive (a–b) occurs between 300 and 350°C. We do not have data for temperatures between 150°C and 200°C or between 300 and 350°C (Table A3.1). Once an earthquake rupture nucleates, it is mechanically favourable for the rupture to propagate into the frictionally weaker siltstone at cooler shallower levels, assuming an identical stress state in both lithologies.

Conclusions

In this research, 2 samples of sandstone and 2 samples of siltstone were collected from immediate hanging wall and footwall of the sinistral-reverse North Leader Fault at Campbell Stream (Figures A1.1, A1.2). Hydrothermal friction experiments were conducted on the greywacke sandstone and siltstone across a wide range of crustal conditions (V=0.01–100 μm s^{-1}, T=20–500°C, and σ_n^{eff}=75 MPa) (Table A3.1) (Figures A3.1, A3.2, A3.3).

Results reveal that at T=250–450°C (12.5 to 22.5 km depth for a 20 °C/km geothermal gradient), all sandstone and siltstone samples have Byerlee (μ=0.6–0.8) values of sliding friction and exhibit velocity-weakening behaviour at sliding velocities between 3 and 30 μm s^{-1} (Figures A3.1, A3.2).

The low temperature velocity-strengthening to velocity-weakening transition, interpreted to represent the shallowest depth of the seismogenic zone, depends on lithology and sliding velocity (Figures A3.2, A3.3). At the lowest velocities imposed (0.01–0.03 μm s^{-1}), the transition from velocity-strengthening to velocity-weakening occurs at 150°C in the sandstone and 200°C in the siltstone. At the highest sliding velocities investigated (30–100 μm s^{-1}), the transition temperature increases to 200°C in the sandstone and 300°C in the siltstone.

The high temperature velocity-weakening to velocity-strengthening transition, interpreted to represent the deepest portion of the seismogenic zone, also depends on lithology and sliding velocity (Figures A3.2, A3.3). At the lowest velocities imposed (0.01–0.03 μm s^{-1}), the transition from velocity-weakening to velocity-strengthening occurs at 400°C in the sandstone and 350°C in the siltstone. At the highest sliding velocities investigated (30–100 μm s^{-1}), the temperature of the transition increases to over 500°C in the sandstone and 450°C in the siltstone.

As shown in the experimental results, frictional stability depends on sliding velocity. Extremely low sliding velocities (0.01-0.03 μm s^{-1}), which are more representative of tectonic plate velocities, correspond with the narrowest temperature range (200–300°C) of velocity-weakening behaviour and unstable slip in *both* the sandstone and siltstone.

Future Work

Our future goal is to identify and model the deformation mechanisms responsible for the three frictional stability regimes observed in the hydrothermal friction experiments. To identify the mechanisms accommodating slip in the friction experiments, additional microstructural observations of the deformed sandstone and siltstone samples are needed. Samples from representative friction experiments are being made into polished thin sections, and we will image them using standard scanning electron microscropy techniques in June 2023.

We have begun to model the experimental results using the microphysical model proposed by Chen and Spiers (2016). The initial models investigated which of the soluble minerals (quartz, potassium feldspar, or albite) most likely controls the observed transitions in the friction rate parameter (a–b). Although the initial results are preliminary and were calculated for single mineral phases, they are encouraging in that they show an initial transition from positive to negative (a–b) at 150–200°C for two of the three minerals modelled, namely quartz and albite. However, additional constraints on grain size and the width of the deforming fault zone are needed for direct extrapolation of the microphysical model to nature.

Finally, extrapolation of the model results to nature will require better constraints on the geothermal gradient, defined as the change in temperature with depth, across New Zealand. This will enable us to convert the experimental temperature range to a depth range, which can then be compared with seismological observations of earthquake occurrence and used in future models of fault behaviour.

Outputs and Dissemination

Boulton, C. (2023), Greywacke: subjectively stunning, frictionally fascinating, and societally relevant. *Victoria University of Wellington Earth Science Seminar*, 8 March 2023.

Boulton, C. (2022), Greywacke: frictionally fascinating and societally relevant. *University of Oklahoma School of Geosciences seminar*, 01 September 2022.

Boulton, C. (2022), Greywacke: subjectively stunning, frictionally fascinating, and societally relevant. *Combined University of Otago–Geoscience Society of New Zealand Otago Branch seminar*, 11 May 2022.

Chua, T.J., S. Ellis, **C. Boulton**, S. Bannister, D. Eberhart-Phillips, A. Niemeijer (2022), Estimating fault rupture depths in the Wellington Region: constraints from laboratory experiments, seismic relocation of earthquake depths and thermal modelling, Geoscience Society Annual Conference, 29 Nov – 1 Dec 2022, *Geoscience Society of New Zealand Miscellaneous Publication 16A*.

Publications and Communications

Publications:

Ellis, S.M., S. Bannister, R. J. Van Dissen, D. Eberhart-Phillips, C. Holden, **C. Boulton**, M. E. Reyners, R. H. Funnell, N. Mortimer, and P. Upton (2021). New Zealand Fault Rupture Depth Model v1.0: a provisional estimate of the maximum depth of seismic rupture on New Zealand's active faults. GNS Science Report 2021/08. Lower Hutt, New Zealand: GNS Science.

Boulton, C., A.R. Niemeijer, S. Ellis, and A. Nicol (in prep). Hydrothermal frictional properties of lithologically heterogeneous bedrock: Effects on earthquake nucleation and rupture propagation. For submission to *Bulletin of the Seismological Society of America*.

Ellis, S.M., S. Bannister, R. J. Van Dissen, D. Eberhart-Phillips, C. Holden, **C. Boulton**, M. E. Reyners, R. H. Funnell, N. Mortimer, P. Upton, C. Rollins, and H. Seebeck (in prep). New Zealand Fault-Rupture Depth Model v1.0: a provisional estimate of the maximum depth of seismic rupture on New Zealand's active faults. For submission to *Seismological Research Letters*.

Media appearances:

- Radio New Zealand's *Our Changing World* ("Finding Faults" 23/02/22; https://www.rnz.co.nz/national/programmes/ourchangingworld/audio/2018831486/finding-faults-and-eavesdropping-on-earthquakes)
- Radio New Zealand's *Nine to Noon* ("Cracking the Mystery of Earthquake Faults" 29/04/22; https://www.rnz.co.nz/national/programmes/ninetonoon/audio/2018839940/greywacke-cracking-the-mystery-of-earthquake-faults)
- Newshub Live at 6 pm ("Common rocks may hold the secret to forecasting future earthquakes" 16/04/22; https://www.newshub.co.nz/home/new-zealand/2022/04/common-rocks-may-hold-the-secret-to-forecasting-future-earthquakes.html).
- An EQC press release ("Greywacke rock research unlocks secrets of earthquake faults" 13/04/22) was published in multiple regional newspapers.

I collaborated with Julian Thomson from Out There Learning on the (greywacke) Wairarapa Fault on the popular YouTube Video: "The Greatest Ever On-Land Fault Movement", published in May 2022 (https://www.youtube.com/watch?v=LUsIIJwxPYU). It has already gained over 300,000 views.

In addition, I have a popular Instagram account (@disaster.averted), where I regularly post stories and details of my greywacke research.

References

Allis, R.G., R.H. Funnell, and X. Zhan (1998). From basins to mountains and back again: NZ basin evolution since 10 Ma. In G.B. Arehart and J.R. Hulston, editors, *Water-rock interaction: proceedings of the 9th International Symposium on Water-Rock Interaction*. 3 April 1998, Taupo, New Zealand. Rotterdam, A.A. Balkema, pp. 3–9.

Ampuero, J.P. and A.M. Rubin (2008). Earthquake nucleation on rate and state faults – Aging and slip laws. *Journal of Geophysical Research: Solid Earth*, 113(B1).

Behnsen, J. and D.R. Faulkner (2012). The effect of mineralogy and effective normal stress on frictional strength of sheet silicates. *Journal of Structural Geology*, 42, 49–61.

Blanpied, M.L., D.A. Lockner, and J.D. Byerlee (1995). Frictional slip of granite at hydrothermal conditions, *Journal of Geophysical Research*, 100(B7), 13,045–13,064, https://doi.org/10.1029/95JB00862.

Boulton, C., A. R. Niemeijer, C. J. Hollis, J. Townend, M. D. Raven, D. K. Kulhanek, and C. L. Shepherd (2019). Temperature-dependent frictional properties of heterogeneous Hikurangi Subduction Zone input sediments, ODP Site 1124. *Tectonophysics*, https://doi.org/10.1016/j.tecto.2019.02.006.

Byerlee, J.D. (1978). Friction of rocks. *Pure and Applied Geophysics*, 116, 615–626.

Chemberlain, C.J., W.B. Frank, F. Lanza, J. Townend, E. Warren-Smith (2021). Illuminating the pre-, co-, and post-seismic phases of the 2016 M7.8 Kaikōura Earthquake with 10 years of seismicity. *Journal of Geophysical Research: Solid Earth*, 126, e2021JB022304, https://doi.org/10.1029/2021JB022304.

Chen, J. and Spiers, C.J. (2016). Rate and state frictional and healing behavior of carbonate fault gouge explained using microphysical model. *Journal of Geophysical Research: Solid Earth*, 121, 8642–8665, https://doi.org/10.1002/2016JB013470.

Chester, F.M., and N.G. Higgs (1992). Multimechanism friction constitutive model for ultrafine quartz gouge at hypocentral conditions, *Journal of Geophysical Research*, 97(B2), 1859–1870, https://doi.org/10.1029/91JB02349.

den Hartog, S.A.M., A.R. Niemeijer, and C.J. Spiers (2012). New constraints on megathrust slip stability under subduction zone P-T conditions, *Earth and Planetary Science Letters*, 353–354, 240–252.

den Hartog, S. and Spiers, C.J. (2014). A microphysical model for fault gouge friction applied to subduction megathrusts. *Journal of Geophysical Research: Solid Earth*, 119, 1510–1529, https://doi.org/10.1002/2013JB010580.

Dieterich, J.H. (1979). Modeling of rock friction: 1. Experimental results and constitutive equations. *Journal of Geophysical Research*, 84(B5), 2161–2168.

Ellis, S.M., S. Bannister, R. J. Van Dissen, D. Eberhart-Phillips, C. Holden, C. Boulton, M. E. Reyners, R. H. Funnell, N. Mortimer, P. Upton (2021). New Zealand Fault Rupture Depth Model v1.0: a provisional estimate of the maximum depth of seismic rupture on New Zealand's active faults. GNS Science Report 2021/08. Lower Hutt, New Zealand: GNS Science.

Hanks, T.C. and H. Kanamori (1979). A moment magnitude scale. *Journal of Geophysical Research*, 84(B5), 2348–2350.

Hubbert, M.K. and W.W. Rubey (1959). Role of fluid pressure in the mechanics of overthrust faulting. *Bulletin of the Geological Society of America*, 70, 115–205.

Litchfield, N., et al. (2018). Surface rupture of multiple crustal faults in the 2016 Mw 7.8 Kaikōura, New Zealand, Earthquake. *Bulletin of the Seismological Society of America*, 108(3B), 1496–1520.

Mackinnon, T.C. (1983). Origin of the Torlesse Terrane and coeval rocks, South Island, New Zealand. *Geological Society of America Bulletin*, 94, 967–985.

Marone, C., Raleigh, C.B. and Scholz, C.H. (1990). Frictional Behavior and Constitutive Modeling of Simulated Fault Gouge. *Journal of Geophysical Research*, 95(B5), 7005–7025.

Moore, D.E. and D.A. Lockner (2004). Crystallographic controls on the frictional behaviour of dry and water-saturated sheet structure minerals. *Journal of Geophysical Research*, 109, B03401.

Moore, D.E., Summers, R. and J.D. Byerlee (1986). The Effects of Sliding Velocity on the Frictional and Physical Properties of Heated Fault Gouge. *Pure and Applied Geophysics*, 124(1/2).

Morrow, C.A., Moore, D.E., and Lockner, D.A. (2017). Frictional strength of wet and dry montmorillonite. *Journal of Geophysical Research: Solid Earth*, 122(5), 3392–3409, https://doi.org/10.1002/2016JB013658.

Morrow, C.A., B. Radney, and J. Byerlee (1992). Frictional strength and the effective pressure law of montmorillonite and illite clays. *Fault Mechanics and Transport Properties of Rocks; a Festchrift in Honor of W.F. Brac*e. San Diego, Academic Press, pp. 60–88.

Mortimer, N. (2004). New Zealand's Geological Foundations. *Gondwana Research*, 7(1), 261–272.

Nicol, A., Khajavi, N., et al. (2018). Preliminary geometry, displacement, and kinematics of fault ruptures in the epicentral region of the 2016 Mw 7.8 Kaikōura, New Zealand, Earthquake. *Bulletin of the Seismological Society of America*, 108(3B), 1521–1539.

Nicol, A., R.J. Van Dissen, M.W. Stirling, and M.C. Gerstenberger (2016). Completeness of the paleoseismic active-fault record in New Zealand. Seismological Research Letters 87(6), 1299–1310.

Niemeijer, A.R. and Spiers, C.J. (2007). A microphysical model for strong velocity weakening in phyllosilicate-bearing fault gouges. *Journal of Geophysical Research*, 112, B10405, https://doi.org/10.1029/2007JB005008.

Niemeijer, A.R., C. Boulton, V.G. Toy, J. Townend and R. Sutherland (2016). Large-displacement, hydrothermal frictional properties of DFDP-1 fault rocks, Alpine Fault, New Zealand: Implication for deep rupture propagation. *Journal of Geophysical Research: Solid Earth*, 121(2), 624–647.

Niemeijer, A.R. (2018). Velocity-dependent slip weakening by the combined operation of pressure solution and foliation development. *Nature Scientific Reports*, 8, 4724, https://doi.org/10.1038/s41598-018-22889-3

Quigley, M., Van Dissen, R., et al. (2012). Surface rupture during the 2010 Mw 7.1 Darfield (Canterbury) earthquake: Implications for fault rupture dynamics and seismic-hazard analysis. *Geology*, 40(1), 55–58.

Renard, F., Dysthe, D., Feder, J., Bjørlykke, K. and Jamtveit, B. (2001). Enhanced pressure solution creep rates induced by clay particles: Experimental evidence in salt aggregates. *Geophysical Research Letters*, 28(7), 1295–1298. https://doi.org/10.1029/2000GL012394

Rutter, E.H., 1976. The kinetics of rock deformation by pressure solution. Philosophical Transactions of the Royal Society of London 283, 203–219.

Rutter, E.H., Mainprice, D.H., 1979. On the possibility of slow fault slip controlled by a diffusive mass transfer process. Gerlands Beiträge zur Geophysik, Leipzig 88, 154–162.

Ruina, A. (1983). Slip instability and state variable laws. *Journal of Geophysical Research*, 88(B12), 10,359–10,370.

Scholz, C.H. (2002), The Mechanics of Earthquakes and Faulting, 2nd ed. Cambridge University Press, Cambridge, 471 pp.

Shaw, B.E., Fry, B., Nicol, A., Howell, A., and M. Gerstenberger (2022). An earthquake simulator for New Zealand. *Bulletin of the Seismological Society of America*, 112, 763–778.

Sibson, R.H. (1985). A note on fault reactivation. *Journal of Structural Geology*, 7(6), 751–754.

Sibson, R.H. (1974). Frictional constraints on thrust, wrench and normal faults. *Nature*, 249, 542–544.

Verberne, B.A., A.R. Niemeijer, J. H.P. De Bresser, and C.J. Spiers (2015). Mechanical behavior and microstructure of simulated calcite fault gouge sheared at 20–600°C: Implications for natural faults in limestones *Journal of Geophysical Research: Solid Earth*, 120, https://doi.org/10.1002/2015JB012292.

Appendices

Appendix 1 Study Locality and Sample Description

The M_w 7.8 Kaikōura Earthquake nucleated on the Humps Fault (west) in North Canterbury. Propagating to the northeast, the earthquake ruptured over 20 faults before finally arresting on the Needles Fault beneath Cook Strait (Litchfield et al., 2018). During the Kaikōura Earthquake, the sinistral-reverse Leader Fault accommodated up to 2.5 ± 0.15 m of horizontal offset and 3.5 ± 0.5 m of vertical offset, with a mean horizontal to vertical slip ratio of 1.4 ± 1.0 (Nicol et al., 2018) (Figure A1.1).

For the mineralogical analysis and hydrothermal friction experiments, samples of sandstone (LF8, LF10) and siltstone (LF6, LF9) were collected from the immediate hanging wall and footwall of the North Leader Fault at Campbell Stream (Figures A1.2). The samples analysed occur within the Late Jurassic-Early Cretaceous Pahau Terrane, a part of the wider Torlesse Composite Terrane (e.g., Mortimer 2004). Additional sample details are provided in the Figure A1.2 caption.

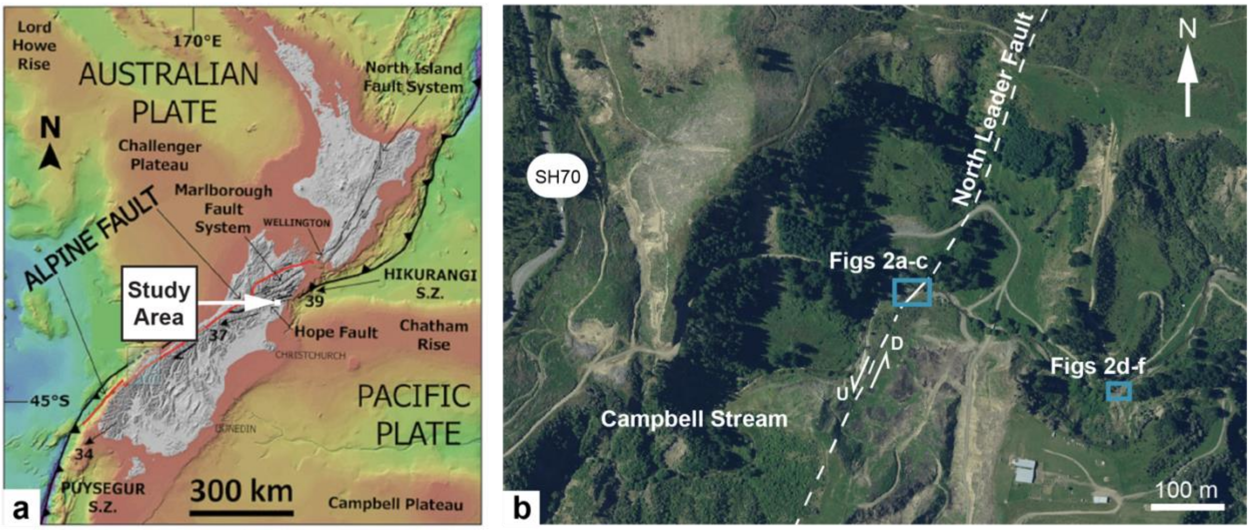

***Figure A1.1**. **(a)** Tectonic setting for the 2016 Kaikōura Earthquake and North Leader Fault. **(b)** Aerial photo, with annotations, of the North Leader Fault at Campbell Stream. The main fault zone is located at 42°28.769´S, 173°15.445´E. Aerial imagery source: Environment Canterbury 2021-2022 Canterbury 0.3 m rural aerial photos.*

***Figure A1.2 (following page).** The North Leader Fault at Campbell Stream. **(a)** Exposure of the fault footwall (FW), principal slip zone (white line with fault kinematic indicators) and hanging wall (HW). View looking southwest. The streambank height at the fault is ~8 m. **(b)** Foliated fault gouge in the immediate HW of the principal slip zone, with inset of siltstone sample LF6 collected from this location. **(c)** Boudinaged sandstone beds in the HW, with inset of sandstone sample LF8 collected from this location. **(d)** Exposure of the FW, from which **(e)** siltstone sample LF9 and **(f)** sandstone sample LF10 were collected. **(g)** Stereogram with fault plane and bedding plane measurements. Note the strong NE-SW trend. Also shown are the tectonically applied principal stress orientations σ_1, σ_2, σ_3.*

Figure A1.2

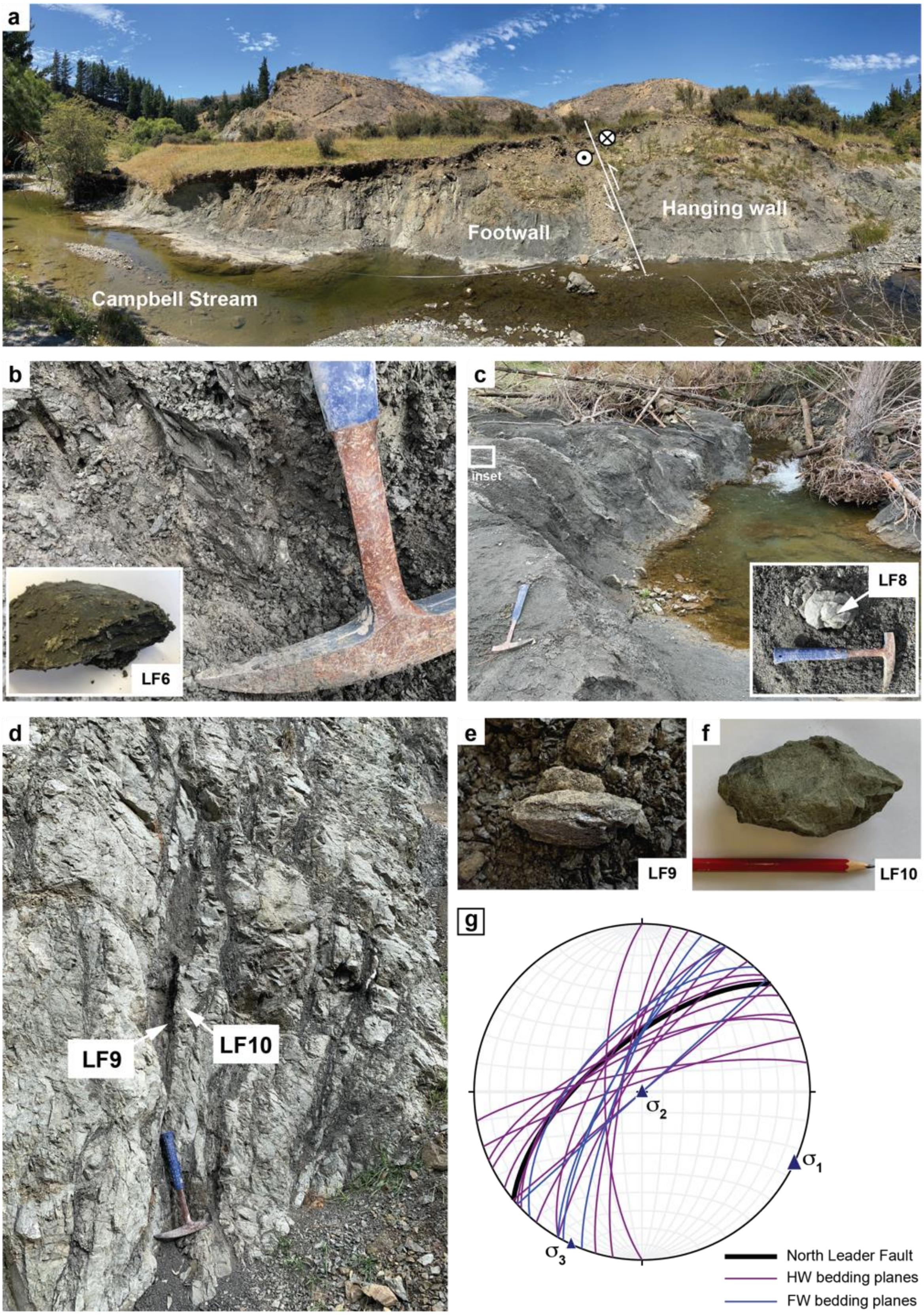
a
Footwall
Hanging wall
Campbell Stream
b
LF6
c
inset
LF8
d
LF9
LF10
e
LF9
f
LF10
g
σ_2
σ_1
σ_3
North Leader Fault
HW bedding planes
FW bedding planes

Appendix 2 Sandstone and Siltstone Mineralogy

Quantitative X-ray diffraction (XRD) analyses were following the methods documented in Boulton et al. (2019). Results are presented in Table A2.1. Approximately 1.5g of each sample was ground for 10 minutes in a McCrone micronizing mill under ethanol. The resulting slurries were oven dried at 60°C and then thoroughly mixed in an agate mortar and pestle before being lightly back pressed into stainless steel sample holders for XRD analysis. The XRD patterns of the micronized samples showed evidence of dehydration of the interlayer of the smectite phase, so they were calcium saturated to restore hydration and maintain a more stable two-water interlayer expansion. This involved dispersing the samples in a 1M $CaCl_2$ solution, centrifuging at 5150g for 10 minutes, calcium saturating a second time, washing with water and then ethanol (centrifuging at 5150g for 10 minutes after each step), and finally oven drying at 60°C. XRD patterns were recorded with a PANalytical X'Pert Pro Multi-Purpose Diffractometer using Fe-filtered Co Kα radiation, automatic divergence slit, 2° anti-scatter slit and fast X'Celerator Si strip detector. The diffraction patterns were recorded from 3 to 80° in steps of 0.017° 2θ with a 0.5 second counting time per step for an overall counting time of approximately 35 minutes. Quantitative analysis was performed on the XRD data using the commercial package SIROQUANT from Sietronics Pty Ltd. The results are normalized to 100%, and hence do not include estimates of unidentified or amorphous materials. All analyses were performed at the Commonwealth Scientific and Industrial Research Organization (CSIRO).

Table A2.1. *Quantitative mineralogy of Leader Fault greywacke sandstone (LF8, LF10) and siltstone (LF6, LF9) samples. K-feldspar denotes potassium feldspar. Ill/Musc denotes illite/muscovite. The smectite mineral is montmorillonite. Other denotes minor phases.*

Sample	Quartz	Plagioclase	K-feldspar	Ill/Musc.	Smectite	Chlorite	Other
LF6	20	24	10	24	13	5	4
LF8	32	36	11	10	5	4	2
LF9	15	26	9	31	7	9	3
LF10	27	39	12	6	4	7	5

Appendix 3 Hydrothermal Friction Experiments

To measure the frictional properties of Leader Fault greywacke siltstone and sandstone samples, hydrothermal friction experiments were performed at Utrecht University following methods described in Niemeijer et al. (2016). In total, 19 experiments were performed; experiment details are documented in Table A3.1. All experiments were performed at a constant effective normal stress (σ_n') of 75 MPa with 50 MPa pore pressure (P_f). Figure A3.1 is a results summary, showing the evolution of the coefficient of sliding friction μ (defined as shear stress / effective normal stress, ignoring cohesion) in 8 experiments on siltstone (LF6, LF9) and sandstone (LF8, LF10) samples.

The four experiments in Figure A3.1a were performed at temperatures stepped from 20 to 100, 200, 250 and 300°C. At each temperature, the simulated gouge was sheared in a series of velocity steps of 1-3-10-30-100 μm s^{-1} to obtain the velocity dependence of friction, expressed as the rate-and-state friction parameter (*a*–*b*). The experiments shown in Figure A3.1b were performed at temperatures stepped from 300 to 350, 400, 450 and 500°C. At room temperature and a velocity *V* of 1 μm s^{-1}, sliding friction μ (hereafter "friction") is lowest for siltstone sample LF6 (μ=0.33), followed by siltstone sample LF9 (μ=0.40)

The siltstone samples both contain >40 wt% phyllosilicates (smectite, illite, muscovite and/or chlorite) (Table A2.1). The two sandstone samples, LF8 and LF10 have less than 20 wt% phyllosilicates, and show comparable friction levels at room temperature (μ = ~0.55). In all experiments, friction increases with increasing displacement and at higher temperatures, but this increase is larger in the siltstone-derived samples so that by the end of the experiments, these samples show the highest friction values. In addition, slip instabilities appear at elevated temperature, starting with sample LF8, which is already frictionally unstable at 200°C, and for all samples at 250°C up to a temperature of 400°C. Sample LF10 shows a few stick-slip instabilities at T=450°C.

The velocity dependence of friction is typically expressed using the parameter (*a*–*b*), defined according to the empirical rate-and-state friction (RSF) laws (Dieterich 1979; Ruina 1983; Ampuero and Rubin 2008):

$$\mu = \mu_0 + aln\left(\frac{V}{V_0}\right) + bln\left(\frac{V_0\theta}{d_c}\right) \tag{1}$$

$$\frac{d\theta}{dt} = 1 - \frac{V\theta}{d_c} \tag{2a}$$

$$\frac{d\theta}{dt} = -\frac{V\theta}{d_c}\ln\left(\frac{V\theta}{d_c}\right) \tag{2b}$$

Here, μ is the coefficient of friction, defined as shear stress/effective normal stress, ignoring cohesion, μ_0 is the coefficient of friction at a reference velocity V_0, V is the instantaneous velocity, *a* is a parameter that quantifies the direct effect, *b* is the parameter that describes the evolution effect, d_c is a characteristic or critical slip displacement over which the state variable, θ, evolves. The state variable θ has units of time and is thought to represent the average lifetime of grain-scale asperity contacts. The RSF equations can be solved for an instantaneous velocity step by combining equation (1) with either of the two state laws in equations (2a) or (2b) and with an equation that describes the elastic interaction of the sample with the loading system. We used a non-linear inversion scheme to find the best fits to the data in which sliding was stable (see Niemeijer et al. 2016 for further details). Solutions of (*a*–*b*) for the Dieterich or slowness law (equation 2a) and for the Ruina or slip law (equation 2b) were the same; solutions yielded differences in the d_c parameter, but these will not be discussed further. In the case of unstable sliding, i.e. stick-slips, we used the approximation that (*a*–*b*) is proportional to the change in friction, $\Delta\mu$, multiplied by ln (V/V_0). The results of our analyses are shown in Figure A3.2.

For all samples, (*a*–*b*) varies significantly with both temperature and velocity. The values at room temperature are predominantly positive, with a few negative values at low velocity for the two sandstone samples LF8 and LF10. As temperature increases, (*a*–*b*) transitions to negative values for all samples. The transition temperature depends on the sample type as well as on velocity. It is around 200°C for the two sandstone samples and 250°C for the two siltstone samples. At the highest velocity investigated (V_1=100 μm s^{-1}), the temperature at which (*a*–*b*) becomes negative is slightly higher, notably for the two siltstone samples LF6 and LF9. A trend of a modest increase in (*a*–*b*) with increasing temperature above 300°C exists, but only sample LF6 showed positive (*a–b*) value again at the 450°C and a velocity V_1 of 3 μm s^{-1} (Figure A3.2).

The seismogenic zone is typically defined as the region in which (*a–b*) is negative, since this is a prerequisite for earthquake nucleation (e.g., Scholz, 2002). Considering the strong velocity dependence of (*a–b*), we decided to expand the investigated range of velocities to 10 nm s^{-1} or 315 mm $year^{-1}$ to more closely simulate the slow loading rates in nature (~5-30 mm $year^{-1}$) and to further investigate the velocity dependence of (*a–b*) instead of investigating the effect of normal stress. We also focused on the transition from negative to positive (*a–b*) that occurs at high temperature, since this transition represents the bottom of the seismogenic zone (e.g., Scholz, 2002). This is typically the depth at which large earthquakes nucleate. The results of these experiments are shown in Figure A3.3. Lowering the velocity by two orders of magnitude leads to a reduction in the temperature at which (*a–b*) transitions from negative to positive values for both samples. That is, the range of temperatures at which earthquakes can nucleate gets narrower. The siltstone sample (LF6) shows positive values at 350°C, while the sandstone sample has its first positive value at 400°C. Moreover, at these elevated temperatures, the variation in (*a–b*) values with velocity is considerable; there is a consistent increase in (*a–b*) with decreasing velocity. There is strong velocity strengthening at low *V* and high *T*, particularly for sample LF6 (note the difference in y-scale between Figures A3.2 and A3.3).

Table A3.1. *Hydrothermal friction experiments, showing experimental ID, sample, temperature (T), effective normal stress (σ_n^{eff}), pore fluid pressure (Pf), velocity (V), and total displacement (x_{final}).*

ID	Sample	T (°C)	σ_n^{eff}(MPa)	Pf (MPa)	*V* (μm s^{-1})	x_{final} (mm)
u873	LF8	20-100-200-250-300	75	50	1-3-10-30-100	59.9
u874	LF9	20-100-200-250-300	75	50	1-3-10-30-100	60.8
u876	LF6	20-100-200-250-300	75	50	1-3-10-30-100	57.9
u878	LF6	300-350-400-450-500	75	50	1-3-10-30-100	56.9
u879	LF8	300-350-400-450-500	75	50	1-3-10-30-100	57.1
u881	LF9	300-350-400-450-500	75	50	1-3-10-30-100	57.9
u882	LF10	20-100-200-250-300	75	50	1-3-10-30-100	57.9
u884	LF10	300-350-400-450-500	75	50	1-3-10-30-100	58.2
u886	LF8	350	75	50	1-0.01-0.03-0.1-0.3-1	10.3
u887	LF6	400	75	50	1-0.01-0.03-0.1-0.3-1	10.2
u889	LF8	400	75	50	1-0.01-0.03-0.1-0.3-1	10.2
u890	LF6	350	75	50	1-0.01-0.03-0.1-0.3-1	10.2
u891	LF8	450	75	50	1-0.01-0.03-0.1-0.3-1	10.2
u892	LF8	500	75	50	1-0.01-0.03-0.1-0.3-1	10.2
u893	LF6	150	75	50	1-0.01-0.03-0.1-0.3-1-3-10-30-100	21.2
u895	LF8	150	75	50	1-0.01-0.03-0.1-0.3-1-3-10-30-100	20.8
u926	LF8	500-550-600	75	50	1-3-10-30-100	
u1069	LF6	200	75	50	1-0.01-0.03-0.1-0.3-1	10.4
u1070	LF6	300	75	50	1-0.01-0.03-0.1-0.3-1	10.4

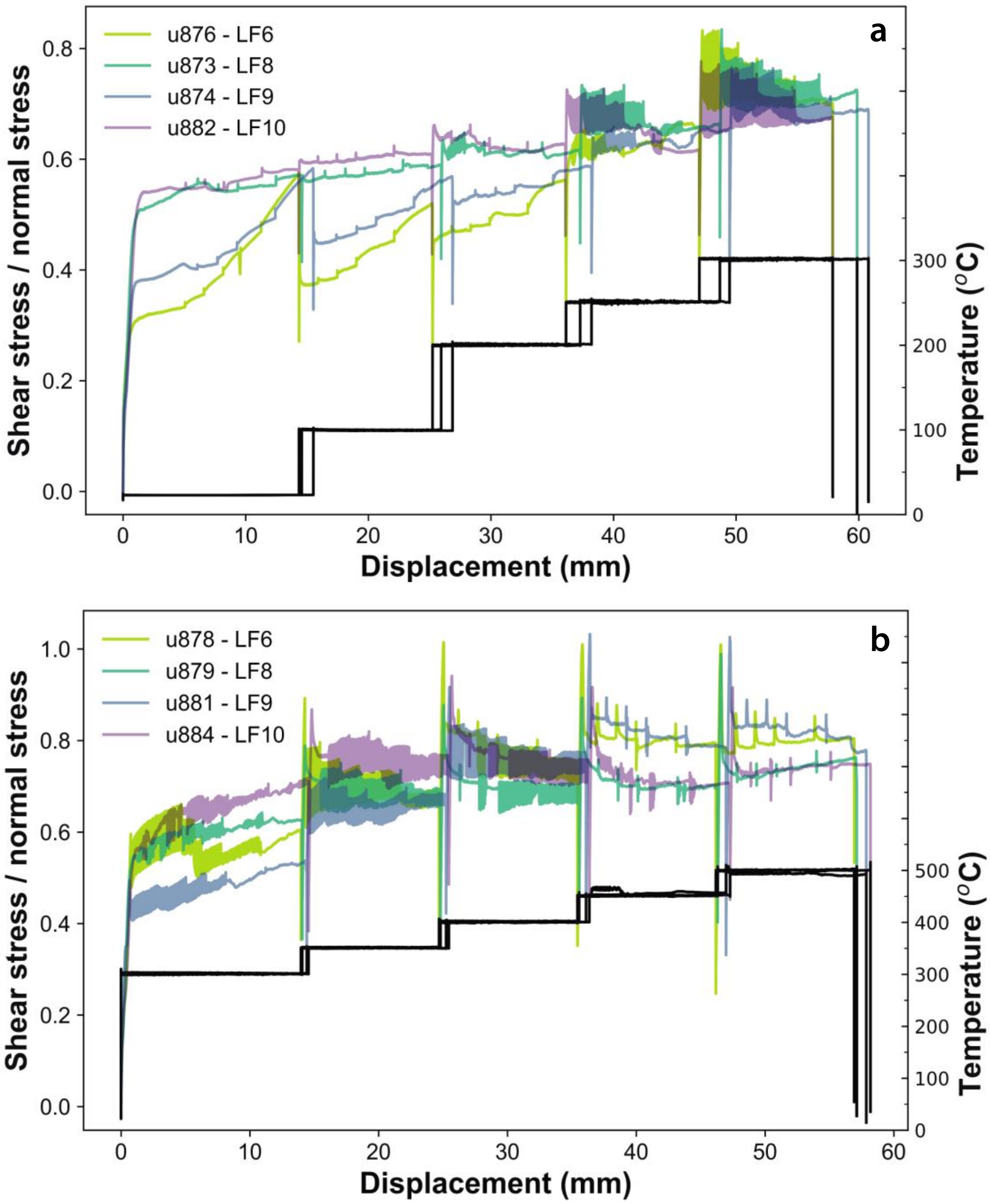

Figure A3.1. *The sliding coefficient of friction μ (shear stress / effective normal stress, ignoring cohesion) as a function of displacement at temperatures ranging from* ***(a)*** *20–300°C and* ***(b)*** *300–500°C. Temperature intervals in which friction shows large variations are showing unstable stick-slips events; these events occur predominantly at 250, 300, 350, and 400°C.*

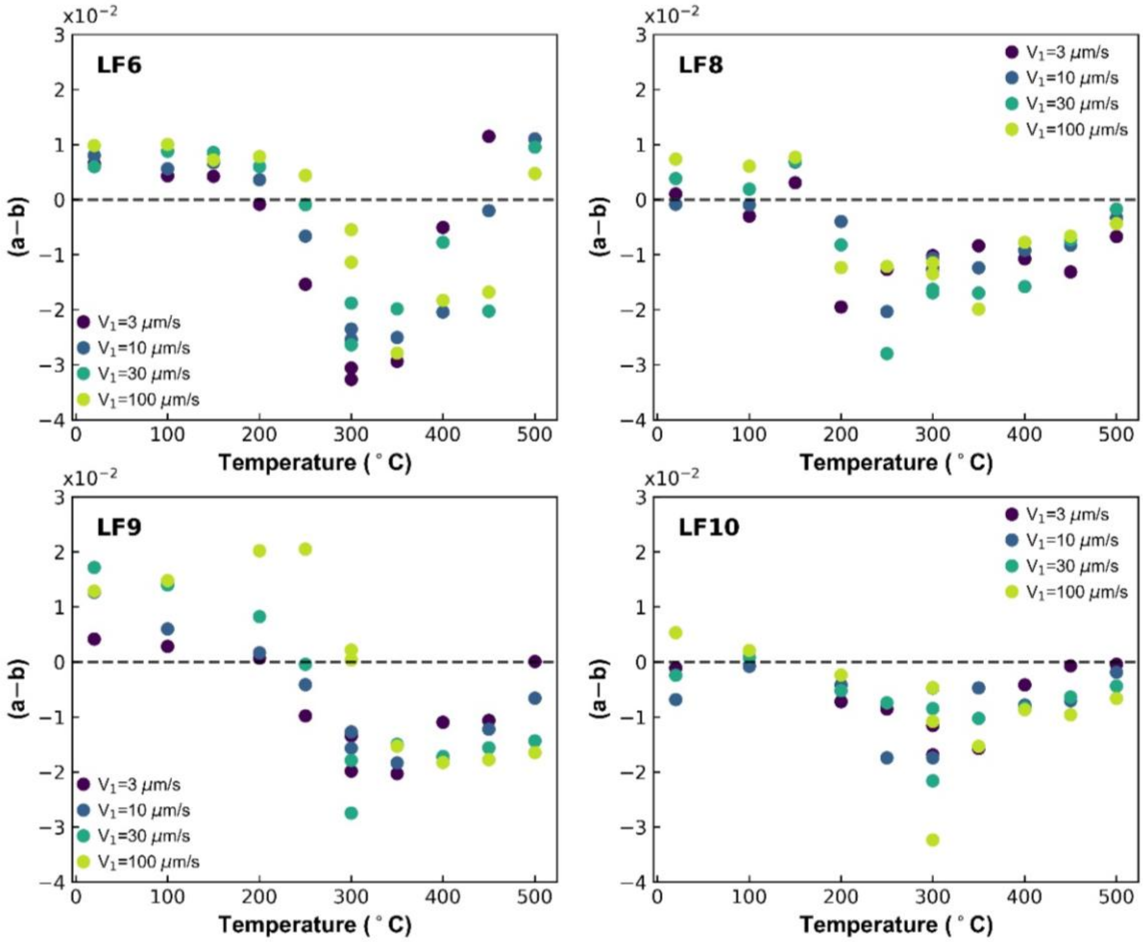

Figure A3.2: *Velocity dependence of friction, expressed as the rate-and-state friction (RSF) parameter (a–b) for all samples as a function of temperature. The data shown are only from the higher velocity experiments. Results show that (a–b) is not a constant; (a–b) has a velocity dependence and a temperature dependence.*

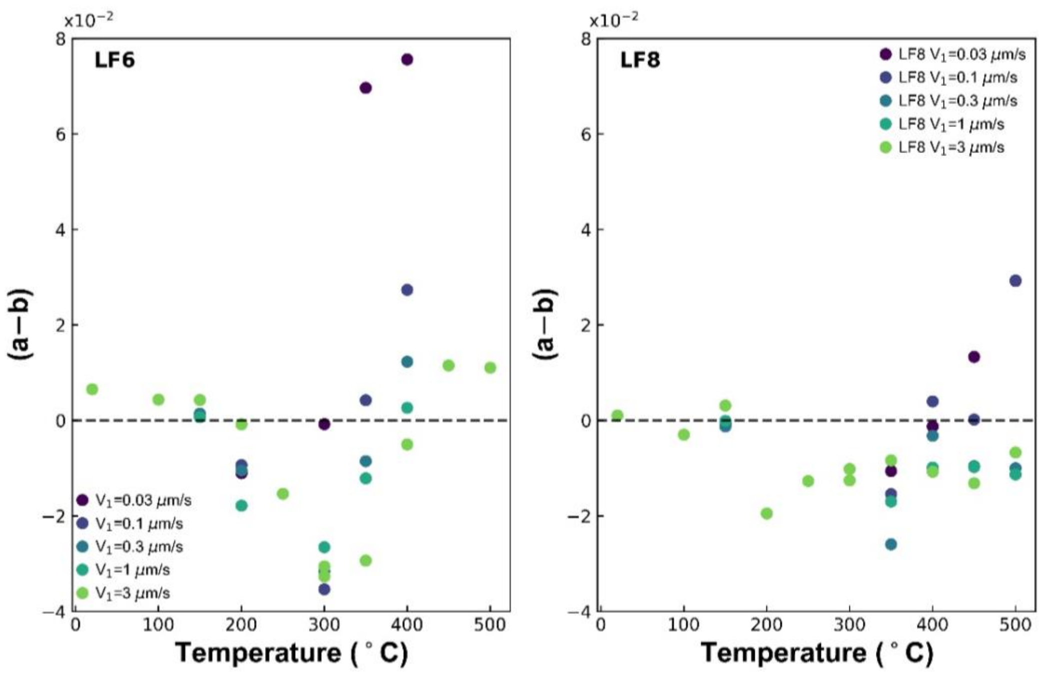

Figure A3.3. *Velocity dependence of friction, expressed as the RSF parameter (a–b), as a function temperature for samples LF6 (siltstone) and LF8 (sandstone). The data shown are only from the lower velocity (slow) experiments.*